Title

A Nanomotor-Based Active Delivery System for Intracellular Oxygen Transport

Journal

ACS Nano, 13(10)

ISSN

1936-0851

Authors

Zhang, Fangyu
Zhuang, Jia
de Ávila, Berta Esteban Fernández
et al.

Publication Date

2019-10-22

DOI

10.1021/acsnano.9b06127

Peer reviewed

Published in final edited form as:

ACS Nano. 2019 October 22; 13(10): 11996–12005. doi:10.1021/acsnano.9b06127.

A Nanomotor-Based Active Delivery System for Intracellular Oxygen Transport

Fangyu Zhang[†], **Jia Zhuang**[†], **Berta Esteban Fernández de Ávila**, **Songsong Tang**, **Qiangzhe Zhang**, **Ronnie H. Fang**, **Liangfang Zhang**[*], **Joseph Wang**[*]

Department of Nanoengineering, University of California San Diego, La Jolla, California 92093, United States.

Abstract

Active transport of gas molecules is critical to preserve the physiological functions of organisms. Oxygen, as the most essential gas molecule, plays significant roles in maintaining the metabolism and viability of cells. Herein, we report a nanomotor-based delivery system that combines the fast propulsion of acoustically-propelled gold nanowire nanomotors (AuNW) with the high oxygen carrying capacity of red blood cell membrane-cloaked perfluorocarbon nanoemulsions (RBC-PFC) for active intracellular delivery of oxygen. The oxygen delivery capacity and kinetics of the AuNW nanomotors carrying RBC-PFC (denoted as "Motor-PFC") are examined under ultrasound field. Specifically, the fast movement of the Motor-PFC under an acoustic field accelerates intracellular delivery of oxygen to J774 macrophage cells. Upon entering the cells, the oxygen loaded in the Motor-PFC is sustainably released, which maintains the cell viability when cultured under hypoxic conditions. The acoustically-propelled Motor-PFC leads to significantly higher cell viability (84.4%) over a 72-hour period, compared to control samples with free RBC-PFC (44.4%) or to passive Motor-PFC (32.7%). These results indicate that the Motor-PFC can act as an effective delivery vehicle for active intracellular oxygen transport. While oxygen is used here as a model gas molecule, the Motor-PFC platform can be readily expanded to the active delivery of other gas molecules to various target cells.

Graphical Abstract

[*]Correspondence to: zhang@ucsd.edu and josephwang@ucsd.edu.

Author Contributions

F. Z., J. Z. contributed equally. The manuscript was written through contributions of all authors. All authors have given approval to the final version of the manuscript.

[†]These authors contributed equally to this work.

The authors declare no competing financial interest.

Supporting Information

The following files are available free of charge *via* the Internet at http://pubs.acs.org.

Acoustic propulsion of motor-PFC at 2 V (Video S1), 4 V (Video S2) and 6 V (Video S3).

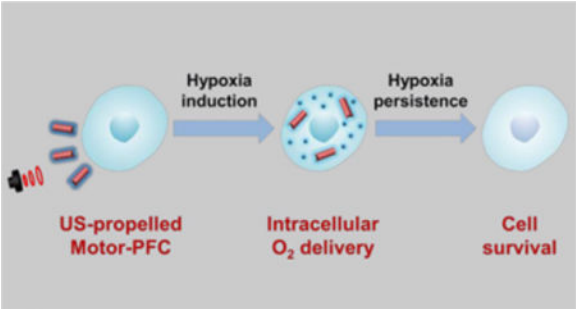

Keywords

oxygen therapy; active delivery; intracellular transport; nanomotor; ultrasound

Gas molecules have essential physiological and pathological roles, impacting various signaling and metabolic pathways. Simple gas molecules such as nitric oxide,[1, 2] carbon monoxide,[3, 4] hydrogen sulfide,[5] and hydrogen[6] have been studied extensively. The transport of gas molecules in appropriate amounts to corresponding tissue sites is critical for positive health outcomes, ranging from heart protection[7] and neuronal repair,[8] to regulation of blood pressure[9] and inflammation.[10] Among a variety of gas molecules being routinely transported during metabolism, oxygen is the most essential for life maintenance. Hypoxia, the decrease in oxygen levels below normal physiological levels, has been shown to play a critical role in the progression of different diseases.[11] The majority of cellular activities requires energy in the form of oxygen, and prolonged and severe hypoxia results in cell death.[12] It is thus crucial to maintain sufficient oxygen availability to cells and tissues.[13] When oxygen levels are critically low, the infusion of donated red blood cells (RBCs) is life-saving measure for patients with significant blood loss. However, due to significant strain on available resources and infrastructure,[14] tremendous efforts have been devoted to the development of viable alternatives to human RBCs for oxygen delivery.[15, 16] Towards this goal, materials with high oxygen solubility have been used as nano/microcarriers for effective blood circulation and deep tissue penetration.[17, 18] In particular, perfluorocarbon (PFC)-based oxygen nanocarriers offer many intrinsic benefits, such as high loading capacity, facile release profile, and relative small size.[19–21] RBC membrane-coated PFC nanoemulsions (RBC-PFC) have recently been reported as a viable candidate for blood substitutes.[22] The formulated biomimetic RBC-PFC could be stored at room temperature for several months and demonstrated high capacity for oxygen delivery. Notably, the RBC-PFC formulation was able to attenuate the effects of hypoxia *in vitro* and could fully resuscitate mice in a model of hemorrhagic shock. The biomimetic surface coating of natural RBC membrane also helped to improve biocompatibility and minimize immunogenicity. Nevertheless, by solely relying on passive circulation and diffusion, the current delivery platforms are not able to actively and effectively localize oxygen to ischemic tissues and hypoxic cells, resulting in suboptimal delivery efficiency.

Over the past decade, researchers have reported on active delivery methods using nano/micromotors, which consist of synthetic nano/microscale structures of different shapes and materials that can convert different energy inputs into mechanical motion.[23–25] The nano/

micromotor field has been growing rapidly and has started to demonstrate great promise for medical applications such as active delivery of therapeutic payloads, fast sensing of important disease markers, accelerated detoxification of human fluids, and cargo-transport towards and into cells.[26–32] Specifically, acoustically-propelled nanomotors have demonstrated major advantages for active intracellular delivery and actuation.[33, 34] These nanomotors are based on gold nanowires (AuNWs), which can display rapid propulsion under an ultrasound (US) field.[32, 35, 36] The gold surface allows facile modification and functionalization of the nanomotors with therapeutic payloads or specific receptors. Then, the acoustic propulsion enables the concentration of nanomotors around target cells, their rapid penetration through cellular membranes, continuous motor motion within the intracellular space, and finally the active delivery of the payloads. Such acoustic propulsion and fast cell internalization have proven useful for accelerating a variety of intracellular processes. For example, US-powered nanomotors have been utilized for rapid intracellular delivery of therapeutic proteins,[37, 38] fast miRNA sensing inside cancer cells,[39] and enhanced siRNA delivery accelerating gene silencing.[40] The capabilities demonstrated by US-propelled nanomotors for active intracellular delivery and actuation shed light on a wide range of potential biomedical applications. Nonetheless, most of the payloads delivered by acoustic nanomotors have been large biomolecules, with no attention given to gas delivery. Thus, we anticipated that combining the mobile nanomotor with an oxygen delivery nanocarrier would lead to the active intracellular delivery of small gas molecules by nanomotor technology.

In this work we describe a nanomotor-based gas delivery strategy for active intracellular oxygen delivery. Our approach took advantage of the combination of the rapid acoustic propulsion of AuNW nanomotors with the high oxygen loading capacity of RBC-PFC, enabling oxygen delivery to the intracellular space of J774 macrophage cells and helping maintain their viability when cultured under hypoxic conditions. Briefly, positively-charged poly-L-lysine (PLL)-modified AuNWs were functionalized with negatively-charged RBC-PFC *via* electrostatic interactions; then, the resulting RBC-PFC loaded nanomotors (denoted as Motor-PFC) were propelled under an US field and actively incorporated into J774 macrophages. Upon entering the cells, the oxygen loaded in the Motor-PFC was sustainably released intracellularly under hypoxic culture conditions, helping to maintain the cell viability against hypoxia. As indicated above, while different platforms have been designed for oxygen delivery, the present active acoustic nanomotor strategy offers significant advantages in terms of cellular penetration and intracellular delivery towards maintaining sufficient oxygen availability to cells. This approach combines the active acoustic motor delivery with the high oxygen-carrying capacity of synthetic PFC and the biocompatibility of the natural cell membrane. These advantages make the Motor-PFC platform an attractive candidate for biomedical application. While the present proof-of-concept study demonstrates active intracellular oxygen delivery to macrophages, a variety of other versatile gas-loaded nanocarriers could be combined with acoustic nanomotors for intracellular delivery of different therapeutic gases.

RESULTS AND DISCUSSION

Figure 1a schematically illustrates the stepwise surface modification of a AuNW nanomotor for the loading of the RBC-PFC oxygen carrier. Initially, the AuNW was functionalized with a self-assembled monolayer of 3-mercaptopropionic acid (MPA), introducing negatively charged carboxyl moieties to the nanomotor surface. A positively charged poly-L-lysine layer was then incorporated onto the AuNW/MPA surface *via* electrostatic interaction. Finally, the RBC-PFC, fabricated according to an early work,[22] were immobilized onto the AuNW/MPA/PLL surface by further electrostatic interaction with the outer PLL layer, leveraging the attraction between the negatively charged RBC membrane surface and the positively charged PLL nanomotor surface. As shown in Figure 1b, the resulting Motor-PFC could be effectively propelled under an acoustic field and actively incorporated into J774 macrophage cells upon a 5 min US treatment. The efficient nanomotor movement under the US field enables effective cell membrane penetration.[38] Upon internalization, the Motor-PFC released the dissolved oxygen under hypoxic culture conditions. The efficiency of the active nanomotor-assisted oxygen delivery could be visualized directly by using fluorescent microscopy. Image-iT Green hypoxia reagent-labelled cells remained nonfluorescent following a 72 h incubation, confirming the oxygen release and prolonged maintenance of the cell viability (Figure 1c, left). In contrast, without the Motor-PFC treatment, the cell displayed a bright fluorescent color, reflecting the significant amount of accumulated hypoxic stress (Figure 1c, right).

The RBC-PFC nanoemulsion formulation is based on the one described earlier with small modifications.[22] The resulting RBC-PFC nanoemulsions have a diameter of ≈170 nm. To gain further insights into the morphology and integrity of the RBC-PFC nanoemulsion, we performed confocal fluorescence imaging of dual-labeled RBC-PFC nanoemulsions (Figure 2a). Scanning electron microscopy (SEM) was carried out to characterize the structural morphology of the Motor-PFC. The SEM imaging (Figure 2b, left) showed that RBC-PFC was bound onto the structure of a AuNW that was 2 μm in length and 400 nm in diameter. Energy-dispersive X-ray (EDX) spectroscopy mapping analysis was also conducted, (Figure 2b) confirming the presence of gold (Au), sulfur (S), phosphorus (P), and fluorine (F), corresponding to the nanomotor core, MPA coating, RBC membrane, and PFC, respectively. To further characterize the efficient RBC-PFC immobilization onto the surface of the AuNW nanomotors, RBC membrane was labeled with the fluorescent dye 1,1′-dioctadecyl-3,3,3′, 3′-tetramethylindodicarbocyanine (DiD) before immobilization onto the AuNW/MPA/PLL nanomotors. Figure 2c shows bright-field, fluorescent (Cy5 channel), and merged images of a group of Motor-PFC (from left to right, respectively). The microscopy images demonstrated the successful immobilization of the DiD-labeled RBC-PFC onto the surface of the AuNW nanomotors. The stepwise surface modification of the AuNW nanomotors was further confirmed by measuring the corresponding zeta potentials (Figure 2d). The introduction of the MPA carboxyl layer was confirmed by the change to a more negative zeta potential value (from −10.4 mV to −25.7 mV). The following modifications with the positively charged PLL and negatively charged RBC-PFC layers were also confirmed by the corresponding zeta potential values (18.1 and −30.1 mV, respectively). The zeta potential value obtained from the resulting Motor-PFC was nearly identical to that observed for RBC-

PFC alone, used as a positive control. These results were in agreement with a previous study on RBC membrane-coated PFC cores.[22] The loading capability of RBC-PFC on AuNWs was evaluated using different amounts of nanomotors (Figure 2e). Samples containing different amounts of nanomotors were incubated with 1 mg/mL of RBC-PFC solution for 1 h, and then the protein content from RBC membrane was calculated. The results demonstrated a gradual protein increase that correlated with the number of nanomotors, from 0.67 μg to 6.5 μg of protein for AuNW nanomotors at concentrations of 6.5×10^4/mL and 5.2×10^5/mL of, respectively.

Next, we characterized the propulsion of Motor-PFC in water under an acoustic field. The propulsion performance of the Motor-PFC was compared to that of the unmodified AuNWs (without RBC-PFC) at different ultrasound voltages. The histogram shown in Figure 3a displays the increase of the average Motor-PFC speed from 28.5 μm/s at 2 V, to 49.8 μm/s at 4 V, to 73.5 μm/s at 6 V. The bare nanomotors displayed overall higher average speeds (53.0, 77.8, and 107.8 μm/s at 2, 4, and 6 V, respectively). The slight speed decrease observed with the Motor-PFC was attributed to the acoustic streaming change around the nanomotor after binding with the RBC-PFC. In low Reynolds number fluid under ultrasound field, the motion of nanomotor is dominated by the Stokes law.[35] The acoustic driving force equals to the Stokes drag force, which can be calculated from the following equation:

$$F_{driving} = F_{stokes} = \frac{2\pi\eta LU}{ln(L/a) - 0.5} \quad (1)$$

Where η is the viscosity coefficient, L and a are the length and radius of Motor-PFC, respectively, and U is the velocity of the motor under ultrasound (6V, 2.66Hz). When RBC-PFC attached to the AuNW, the radius of the Motor-PFC increased to about 350 nm compared to 200 nm of the bare motor. Therefore, as expected from Equation (1), the speed of the Motor-PFC decreased compared to the bare motor under the same acoustic pressure.

Despite the small effect that the loaded RBC-PFC has on the nanomotor propulsion, the movement of the Motor-PFC provided sufficient thrust for effective penetration through the cell membrane for further internalization and delivery of oxygen molecules, as it will be illustrated below. Figure 3b shows representative tracking trajectories of individual Motor-PFC at the different studied voltages within a 1 s interval in water. In accordance to earlier observations, the distance and speed increased dramatically with applied voltage (more than doubling between 2 and 6 V).

The binding stability of the RBC-PFC on the AuNWs after acoustic propulsion was then evaluated (Figure 3c). For this study, DiD-labeled RBC (red) and BODIPY-labeled PFC (green), prepared as in a previous study,[22] were used for nanomotor modification. Microscopic optical and fluorescent images of Motor-PFC before and after applying the acoustic field (top and bottom rows, respectively) were taken. The merged fluorescence images displayed in the top row demonstrate the binding of RBC-PFC onto the AuNW nanomotors (Figure 3c top, in orange). The Motor-PFC was then allowed to propel in water for 5 min under an acoustic field (6 V and 2.66 Hz). The fluorescent and overlay images (Figure 3c bottom, in orange) demonstrate that the RBC-PFC remained stable on the

nanomotor surface following acoustic propulsion, verifying the good stability of the system, as desired for its application for intracellular oxygen delivery.

We further examined the oxygen delivery capacity and kinetics of the Motor-PFC by following our previously reported protocol.[22] Specifically, a volume of water was first deoxygenated by nitrogen purging, and various samples were injected into the closed system. The corresponding dissolved oxygen (DO) levels were monitored over time (Figure 4a). We first evaluated the oxygen release profiles in the absence of an US field. Owing to the high oxygen loading capacity of PFC, Motor-PFC presented similar DO kinetics compared with RBC-PFC (1.7 mg/L) when normalized to the same RBC-PFC content (Figure 4a, empty red circles *versus* empty blue triangles). Based on this oxygen saturated value, we calculated the total loading capacity of our Motor-PFC to be 0.4 pg/motor. In contrast, bare motors displayed a basal level of oxygen release, which was similar to the regular water control (0.7 mg/L), due to the lack of any oxygen loading (Figure 4a, empty purple diamonds). Subsequently, we examined whether the DO kinetics of Motor-PFC could be expedited by applying an US field. Interestingly, the Motor-PFC demonstrated a faster oxygen release pattern under US, reflecting the impact of nanomotor motion in promoting fast mass exchange with the surrounding environment (Figure 4a, red circles). Not surprisingly, in the absence of nanomotor propulsion, free RBC-PFC (not bound to AuNWs) exposed to the US field did not display accelerated DO kinetics (Figure 4a, full blue triangles). On the other hand, despite the fast propulsion of bare AuNWs under the US field, minimal oxygen release was observed under these conditions due to the absence of the RBC-PFC oxygen reservoir (Figure 4a, purple diamonds). We also quantified the time required to reach kinetic equilibrium in each condition (Figure 4b). Here, we define equilibrium as the state when the level of dissolved oxygen reaches a plateau with no further increase. Similarly, we define the time to equilibrium as the time taken to reach such plateau. US-propelled Motor-PFC reached the kinetic equilibrium within 40 s, while more than 80 s were needed under static conditions. Moreover, we compared the DO levels of each sample in the first 40 s, which clearly demonstrated that Motor-PFC under US showed the highest DO level and the most favorable release profile at each examined timepoint (Figure 4c).

Furthermore, we found that the oxygen delivery profiles could be finely manipulated by adjusting the US voltage, as shown in Figure 4d. Specifically, by increasing the applied US voltage, the oxygen could be released into the environment in a faster manner. With the Motor-PFC, it only took 40 s for oxygen levels to reach equilibrium using a 6 V US field, compared to 56 and 72 s for under 4 and 2 V fields, respectively (Figure 4e). In terms of DO levels, Motor-PFC under 6 V US outperformed the nanomotor under lower voltages at each timepoint (Figure 4f). Overall, these results highlight the essential roles of the RBC-PFC and the US propulsion in the hybrid nanomotor system, with the RBC-PFC offering high oxygen loading while the AuNW nanomotors accelerating the oxygen transport and release. Furthermore, these data also demonstrate that the oxygen release rate can be controlled by tuning the US voltage.

After validating the oxygen delivery capability of Motor-PFC bestowed by the synergistic effects of both components (RBC-PFC and US-propelled AuNW), we assessed the ability of this dynamic nanomotor system for intracellular oxygen delivery into hypoxic cells. Murine

J774 macrophages were selected for this study due to their ability to be cultured in suspension, which helps to increase motor-cell contacts and facilitate penetration by US-powered Motor-PFC through the cell membrane and subsequent intracellular oxygen delivery. More importantly, macrophages have high sensitivity to oxygen and prompt response to hypoxia, which has been well characterized by their significant biological functions against inflammation and relationships with tumor growth.[41, 42] In the present experimental setup, the Motor-PFC was first brought to a levitation plane by the acoustic radiation force exerted on the nanowire motor.[43] After levitation, the local acoustic streaming effects arising from the shape asymmetric property of AuNWs can lead to the small amplitude oscillation in a standing wave which is translated into motion of Motor-PFC in a direction perpendicular to the acoustic wave.[44] The motion of Motor-PFC provides thrust towards the cell and the driving force contributes to the active macrophage penetration and internalization.

First, we evaluated the US-driven intracellular oxygen delivery to cells under hypoxic conditions (Figure 5). Specifically, J774 cells were suspended at 4 million cells/mL, followed by the addition of Motor-PFC. Then, the cell/nanomotor suspension was exposed to the US field for 5 min. During the treatment, the ultrasound field provided energy for the Motor-PFC propulsion generating the force beneficial for cell poration. The driving force of the US-powered Motor-PFC can be estimated to be around 2.1pN based on equation (1). After the application of the US field, we tested the viability of the motor-treated cells by a cell proliferation assay and compared it to that of the untreated cells over a given time period, observing minimal difference between the two groups (data not shown). The cells were washed extensively to remove all unbound nanomotors, leaving only the internalized nanomotors for analysis. The ultimate proof for the effective penetration through the cell membrane and subsequent internalization of Motor-PFC into J774 cells has been demonstrated by optical imaging (Figure 5a). For example, the optical image on the left shows clearly that the US-propulsion greatly enhances the Motor-PFC penetration and internalization into J774 cells, as indicated from the presence of several Motor-PFC within the cell. The image was taken right after performing the ultrasound treatment for 5 min. In contrast, no nanomotors were found in J774 cells treated with the same motors but in the absence of ultrasound (Figure 5a right panel), as expected from the short treatment time (5 min).

The cells were then cultured under hypoxic conditions for varying amounts of time (*i.e.* 24, 48, 72 h), and the effects on cell viability were assessed by a MTS cell viability assay. Notably, the active Motor-PFC was capable of preserving cell viability even after long periods of hypoxia induction, with near 85% cell recovery throughout the study (Figure 5b, red line). In contrast, only ~30–40% cell recovery was observed over a 72-h period for all control groups, including the RBC-PFC under US (*i.e.* without the AuNW carrier). We attributed the benefits (85% cell recovery) of the US-driven Motor-PFC system to the sustained oxygen release from the internalized nanomotors. Under hypoxic conditions, the nanomotors localizing in the cytoplasm could release sufficient oxygen to mitigate the negative effects. In contrast, without applying the US field, most of the Motor-PFC in suspension would be removed, leading to an inability to maintain the cell viability. In contrast, RBC-PFC is not able to achieve such restoration efficiency since it could not

effectively penetrate the plasma membrane. Only a small portion of RBC-PFC was attached to the cells during the US treatment, resulting in slightly improved cell viability. Although bare motors could penetrate cell plasma membrane, they lacked RBC-PFC and oxygen delivery capacity. The intracellular oxygen delivery efficiency to hypoxic cells was also visualized fluorescently by staining the cells with a commercial detection reagent (Figure 5c). In general, significant fluorescent signals were observed in cells subjected to hypoxia over time, and only the intracellular oxygen delivery by US-driven Motor-PFC resulted in the absence of this signal. The two data sets do show good correlation: whereas cells without any treatment present most hypoxic stress and lower the cell survival, the Motor-PFC-treated cells demonstrate minimum hypoxic stress and best survival. Thus, the relief of hypoxia should be the main reason for the significantly higher viability of the cells treated by Motor-PFC under US, highlighting again the significant role of the active oxygen delivery capability of the Motor-PFC. Finally, we evaluated the impact of Motor-PFC concentration on the protective effects of the formulation (Figure 5d). At the highest concentration tested, minimal reduction in cell viability was observed. Fluorescence microscopy measuring hypoxia levels matched well with the cell viability data (Figure 5e). It is noteworthy that the intracellular delivery efficiency could be further optimized by increasing the loading of RBC-PFC onto the AuNWs or by adding more Motor-PFC to the cell suspension.

CONCLUSIONS

We have presented an effective method to actively deliver oxygen inside living cells using US-propelled nanomotors modified with biomimetic RBC-PFC nanoemulsions. The RBC-PFC, possessing a high oxygen loading capacity, was readily functionalized onto the nanomotor surface without affecting the acoustic propulsion. Oxygen release kinetic studies indicated that the US-driven Motor-PFC formulation could release oxygen significantly faster compared to other controls (*i.e.* same Motor-PFC under static conditions). The oxygen release rate could also be tuned by adjusting the ultrasound intensity. We also confirmed that the combination of synthetic AuNW nanomotors with oxygen-carrying RBC-PFC nanoemulsions enabled direct and efficient intracellular oxygen delivery inside J774 macrophage cells, which significantly improved cell viability. Notably, the Motor-PFC could penetrate through the cell membrane and deliver oxygen into cells under hypoxia, maintaining 85% cell viability after 72 h, compared to 45% with free RBC-PFC and 30% with their static counterparts. Such motor-based oxygen delivery could also be used to target other cell types, such as tumor cells for therapeutic purposes like photodynamic therapy and cardiac muscle cells for myocardial oxygen consumption. While this nanomotor-based intracellular delivery platform is still in its early stage and future system optimization is needed before leveraging this delivery strategy into clinical settings, this proof-of-concept work clearly demonstrates the advantages of the nanomotor-based system for *in vitro* intracellular oxygen delivery. Future studies will aim at optimizing this nanomotor-based oxygen delivery system towards application at local hypoxic tissue sites. Meanwhile, these findings demonstrate that Motor-PFC can act as a powerful oxygen delivery vehicle with considerable promise for future therapeutic applications. While oxygen was selected here as a model gas molecule, we anticipate that this work will encourage the nanomotor-based dynamic intracellular delivery of other therapeutic gas molecules towards diverse biomedical

applications. By reducing the size of the AuNW motors, switching to other biocompatible motor systems or discovering alternative active delivery mechanisms, we envision it is possible to design advanced motor systems for oxygen delivery in more practical scenarios.

MATERIALS AND METHODS

Reagents and materials

Polycarbonate (PC) membranes (400 nm pore size) were supplied from Whatman (cat. No. 110407). Gold and silver-plating solutions (Orotemp 24 RTU RACK and 1025 RTU at 4.5 Troy/gallon) were purchased from Technic Inc. (Anaheim, CA). 3-mercaptopropionic acid (MPA), poly-L-lysine (PLL) and PFC (perfluorooctyl bromide) were purchased from Sigma-Aldrich. Methylene chloride (HPLC grade) was obtained from Fisher Scientific. Human O-positive RBCs were obtained from the San Diego Blood Bank. DiD (1,1'-dioctadecyl-3,3,3', 3'-tetramethylindodicarbocyanine perchlorate) and Image-iT Green hypoxia reagent were obtained from Invitrogen. BODIPY PFC staining dye was synthesized using a previous reported approach.[45] J774 macrophages (TIB-67; American Type Culture Collection) were maintained in Dulbecco's modified Eagle medium (HyClone) supplemented with 10% fetal bovine serum (HyClone) and 1% penicillin-streptomycin (Gibco). CellTiter AQ_{ueous} One Solution cell proliferation assay was obtained from Promega.

Preparation of AuNW nanomotor

The AuNW nanomotors were fabricated by a template-assisted electrodeposition method. A 400-nm diameter porous PC membrane was first sputtered with a thin layer of gold. The membrane was then assembled in a Teflon plating cell and served as a working electrode using aluminum foil as an electrical contact for subsequent electrodeposition. A thin sacrificial silver layer was initially electrodeposited into the PC membrane using a charge of 0.1 C and a potential of −0.9 V (*versus* Ag/AgCl reference electrode, and a Pt wire as a counter electrode). Then, Au was electroplated using a gold plating solution at −1 V (*versus* Ag/AgCl) with a charge of 2 C. The sputtered gold layer was removed by mechanical polishing with cotton tip applicators soaked with 3–4 μm aluminate powder. The silver sacrificial layer was then removed by a quick chemical etching using 8 M HNO_3 solution. The removal of this sacrificial layer helped to form the concave shape in one end of the AuNW. Subsequently, the membrane was dissolved in a pure methylene chloride solution for 30 min under vigorous shaking for complete release of the AuNWs. The resulting nanomotors were separated from the solution by centrifugation at 4600 *g* for 3 min and washed twice with isopropanol, ethanol and ultrapure water. Between each step, the nanomotor was mixed with desired solvent and briefly sonicated to ensure the complete dispersion in the solvent. All AuNWs were stored in 1 mL of ultrapure water at room temperature until use.

Preparation of RBC-PFC

RBC-PFC was prepared following a previously reported method.[22] Specifically, RBC membrane ghosts were obtained by hypotonic lysis. The RBC membrane was suspended at a final protein concentration of 2 mg/mL. To prepare RBC-PFC, 50 μL of the PFC was mixed with 2 mL of RBC membrane solution, followed by emulsification on ice using Fisher

Scientific 150E Digital Sonic Dismembrator for 2 min with an on/off interval of 2 s/1 s. The resulting RBC-PFC was centrifuged at 600 *g* for 5 min to remove the excess of membrane vesicles, followed by resuspension in 1 mL of water. For fluorescent imaging of the RBC-PFCs, dual-labeled samples were immobilized on glass slides with Tissue-Tek OCT compound (Sakura Finetek) and visualized using an Olympus FV1000 confocal microscope.

Preparation of Motor-PFC

Motor-PFCs were prepared by the immobilization of the RBC-PFC onto the surface of AuNWs. Firstly, 100 μL of AuNWs were mixed with 5 μL of 11.5 M MPA solution and kept stirring overnight to successfully form the self-assembly monolayer (SAM) onto the nanomotor surface. The resulting MPA-AuNWs were washed twice with ultrapure water and then incubated with 100 μL of a 0.01% PLL solution for 2 h under vigorous shaking, aiming to obtain a positively charged PLL coating on the AuNWs. Finally, the resulting PLL-AuNWs were incubated with 100 μL RBC-PFC at 37 °C for 1 h to obtain Motor-PFC. The nanomotors were washed with ultrapure water between each modification step (centrifuging at 4600 *g* for 3 min).

Characterization of Motor-PFC

SEM image of Motor-PFC was obtained with a Zeiss Sigma 500 scanning electron microscope instrument using an acceleration voltage of 10 KV. EDX mapping analysis was performed using an Oxford EDX detector attached to SEM instrument and operated by Pathfinder software. Brightfield and fluorescent images of Motor-PFC modified with BODIPY labeled PFC and DiD labeled RBC membrane were captured using an EVOS FL microscope. Zeta potential measurements were conducted by a Malvern Instruments Zetasizer Nano ZS. The RBC-PFC loading was determined by Pierce BCA protein assay kit (Thermo Scientific).

Ultrasound equipment and propulsion studies

The acoustic cell setup consisted of a piezoelectric transducer (Ferroperm PZ26 disk 10 mm diameter, 0.5 mm thickness) responsible for the generation of ultrasound waves, attached by conductive epoxy glue to the bottom center of a steel plate ($50 \times 50 \times 0.94$ mm^3); then the steel plate was covered with a 240 μm Kapton tape protective layer and a sample reservoir at the center (5 mm). A glass slide was used to cover the reservoir for ultrasound reflection and to protect the sample. The continuous ultrasound sine wave was applied *via* a piezoelectric transducer, through an Agilent 15 MHz arbitrary waveform generator, in connection to a homemade power amplifier. All propulsion experiments were conducted by applying a continuous sine wave form that had a frequency of 2.66 MHz and an amplitude of 2.0 V, 4.0 V or 6.0 V (voltage at the output of the function generator). Videos were captured using a Cool SNAP HQ^2 camera, with 20× and 40× objectives and acquired at 10 frames per second using the Metamorph 7.1 software (Molecular Devices, Sunnyvale, CA). The particle displacement image stacking was performed using ImageJ software and Flow Trace Plugin.

Dissolved oxygen kinetics

A measurement apparatus was built by a 20 mL glass vial with a foam cap, which was sealed in place using Parafilm (Bemis). Three holes were cut into the foam cap in order to accommodate with a syringe for nanomotor injection, an oxygen probe, and a plastic pipette for degassing. An acoustic cell setup was attached by conductive epoxy glue to the bottom center of the glass vial. Before the start of each experiment, 1 mL of water was added to the vial, and purged with nitrogen to remove dissolved oxygen. When dissolved oxygen meter was stable, 1 mL of Motor-PFC was injected into the bottom of vial under ultrasound with a frequency of 2.66 MHz and an amplitude of 6.0 V. The control experiment (RBC-PFC or bare motor) with ultrasound was conducted under the same conditions as Motor-PFC with normalized concentration. The static controls, oxygen release of Motor-PFC, RBC-PFC, bare motor and water without ultrasound were employed in the same condition. Intensity-dependent oxygen release of Motor-PFC was conducted at various amplitudes (2.0 V, 4.0 V and 6.0 V; keeping the frequency constant at 2.66 MHz).

Intracellular oxygen delivery

J774 cells cultured in suspension (2.5 μL, containing ~10000 cells) were treated with Motor-PFC (2.5 μL, 1.3×10^4 motors) during 5 min in the ultrasound setup (6 V, 2.66 MHz, 5 min). The 5 min treatment time was chosen based on previous reports.[38] In order to obtain enough cells for the following studies, the US treatment was repeated multiple times (20 times) for every control experiment, and the treated cells were combined at the very end. The resulting cell–nanomotor suspension (~100 μL) was collected in an Eppendorf tube. After leaving undisturbed for 5 min at room temperature, the unbound Motor-PFC was removed and the settled cells were resuspended in 100 μL DMEM medium. An EVOS FL microscope with 100X oil objective lens was used to image the motor internalization to the cells. 5 μL of cells were transferred to the well of a 96-well plate containing 95 μL culturing medium. The cells were then incubated under hypoxic conditions (1% O_2/5% CO_2/94% N_2) in a Thermo Scientific Forma Series 3 WJ incubator. Cells were examined at certain timepoints (*i.e.* 24 h, 48 h, 72 h) by cell viability assay and hypoxia imaging. Specifically, cell viability was quantified using a CellTiter AQ_{ueous} One Solution cell proliferation assay (Promega) following the manufacturer's instructions, and cells were stained by Image-iT Green hypoxia reagent and imaged using an EVOS FL microscope. Normoxic control cells were incubated under normoxic conditions (20% O_2/5% CO_2/75% N_2) in a Thermo Scientific Heracell 150i incubator. For static control of Motor-PFC, the ultrasound treatment was omitted.

Supplementary Material

Refer to Web version on PubMed Central for supplementary material.

ACKNOWLEDGMENTS

This work was supported by the Defense Threat Reduction Agency Joint Science and Technology Office for Chemical and Biological Defense (Grant Numbers HDTRA1-13-1-0002 and HDTRA1-14-1-0064), and by the National Institutes of Health under Award Number R01CA200574.

REFERENCES

1. Wang R Gasotransmitters: Growing Pains and Joys. Trends Biochem. Sci 2014, 39, 227–232. [PubMed: 24767680]
2. Carpenter AW; Schoenfisch MH, Nitric Oxide Release: Part II. Therapeutic Applications. Chem. Soc. Rev 2012, 41, 3742–3752. [PubMed: 22362384]
3. Motterlini R; Otterbein LE, The Therapeutic Potential of Carbon Monoxide. Nat. Rev. Drug Discov 2010, 9, 728–743. [PubMed: 20811383]
4. García-Gallego S; Bernardes GJL, Carbon-Monoxide-Releasing Molecules for the Delivery of Therapeutic CO In Vivo. Angew. Chem. Int. Ed 2014, 53, 9712–9721.
5. Cooper CE; Brown GC, The Inhibition of Mitochondrial Cytochrome Oxidase by The Gases Carbon Monoxide, Nitric Oxide, Hydrogen Cyanide and Hydrogen Sulfide: Chemical Mechanism and Physiological Significance. J. Bioenerg. Biomembr 2008, 40, 533–539. [PubMed: 18839291]
6. Ohsawa I; Ishikawa M; Takahashi K; Watanabe M; Nishimaki K; Yamagata K; Katsura K-i.; Katayama, Y.; Asoh, S.; Ohta, S., Hydrogen Acts as A Therapeutic Antioxidant by Selectively Reducing Cytotoxic Oxygen Radicals. Nat. Med 2007, 13, 688–694. [PubMed: 17486089]
7. Andreadou I; Iliodromitis EK; Rassaf T; Schulz R; Papapetropoulos A; Ferdinandy P, The Role of Gasotransmitters NO, H_2S and CO in Myocardial Ischaemia/Reperfusion Injury and Cardioprotection by Preconditioning, Postconditioning and Remote Conditioning. Br. J. Pharmacol 2015, 172, 1587–1606. [PubMed: 24923364]
8. Shefa U; Yeo SG; Kim M-S; Song IO; Jung J; Jeong NY; Huh Y, Role of Gasotransmitters in Oxidative Stresses, Neuroinflammation, and Neuronal Repair. BioMed Res. Int 2017, 2017, 1–15.
9. Zoccali C; Catalano C; Rastelli S, Blood Pressure Control: Hydrogen Sulfide, A New Gasotransmitter, Takes Stage. Nephrol. Dial. Transplant 2009, 24, 1394–1396. [PubMed: 19228755]
10. Shatalin K; Shatalina E; Mironov A; Nudler E, H_2S: A Universal Defense Against Antibiotics in Bacteria. Science 2011, 334, 986–990. [PubMed: 22096201]
11. Owen J; McEwan C; Nesbitt H; Bovornchutichai P; Averre R; Borden M; McHale AP; Callan JF; Stride E, Reducing Tumour Hypoxia via Oral Administration of Oxygen Nanobubbles. PLoS One 2016, 11, e0168088. [PubMed: 28036332]
12. Harris AL, Hypoxia — A Key Regulatory Factor in Tumour Growth. Nat. Rev. Cancer 2002, 2, 38–47. [PubMed: 11902584]
13. Vincent J-L; De Backer D, Oxygen Transport—The Oxygen Delivery Controversy. Intensive Care Med. 2004, 30, 1990–1996. [PubMed: 15258731]
14. Beliën J; Forcé H, Supply Chain Management of Blood Products: A Literature Review. Eur. J. Oper. Res 2012, 217, 1–16.
15. Buehler PW; D'Agnillo F; Schaer DJ, Hemoglobin-Based Oxygen Carriers: from Mechanisms of Toxicity and Clearance to Rational Drug Design. Trends Mol. Med 2010, 16, 447–457. [PubMed: 20708968]
16. Castro CI; Briceno JC, Perfluorocarbon-Based Oxygen Carriers: Review of Products and Trials. Artif. Organs 2010, 34, 622–634. [PubMed: 20698841]
17. Riess JG, Oxygen Carriers ("Blood Substitutes") Raison d'Etre, Chemistry, and Some Physiology Blut ist ein ganz besondrer Saft. Chem. Rev 2001, 101, 2797–2920. [PubMed: 11749396]
18. Winslow RM, Blood Substitutes. Adv. Drug Deliv. Rev 2000, 40, 131–142. [PubMed: 10837785]
19. Riess JG, Perfluorocarbon-based Oxygen Delivery. Artif. Cells Blood Substit. Biotechnol 2006, 34, 567–580.
20. Lowe KC, Engineering Blood: Synthetic Substitutes from Fluorinated Compounds. Tissue. Eng 2003, 9, 389–399. [PubMed: 12857407]
21. Riess JG, Understanding The Fundamentals of Perfluorocarbons and Perfluorocarbon Emulsions Relevant to In Vivo Oxygen Delivery. Artif. Cells Blood Substit. Biotechnol 2005, 33, 47–63.
22. Zhuang J; Ying M; Spiekermann K; Holay M; Zhang Y; Chen F; Gong H; Lee JH; Gao W; Fang RH; Zhang L, Biomimetic Nanoemulsions for Oxygen Delivery In Vivo. Adv. Mater 2018, 30, 1804693.
23. Wang J, Nanomachines: Fundamentals and Applications. Wiley-VCH; Weinheim, Germany, 2013.

24. Wang H; Pumera M, Emerging Materials for The Fabrication of Micro/Nanomotors. Nanoscale 2017, 9, 2109–2116. [PubMed: 28144663]
25. Chen X-Z; Hoop M; Mushtaq F; Siringil E; Hu C; Nelson BJ; Pané S, Recent Developments in Magnetically Driven Micro- and Nanorobots. Appl. Mater. Today 2017, 9, 37–48.
26. Li J; Esteban-Fernández de Ávila B; Gao W; Zhang L; Wang J, Micro/Nanorobots for Biomedicine: Delivery, Surgery, Sensing, and Detoxification. Sci. Robot 2017, 2, eaam6431. [PubMed: 31552379]
27. Gao W; de Ávila BE-F; Zhang L; Wang J, Targeting and Isolation of Cancer Cells Using Micro/Nanomotors. Adv. Drug Deliv. Rev 2018, 125, 94–101. [PubMed: 28893551]
28. Esteban-Fernández de Ávila B; Angsantikul P; Li J; Gao W; Zhang L; Wang J, Micromotors Go In Vivo: From Test Tubes to Live Animals. Adv. Funct. Mater 2018, 28, 1705640.
29. Chałupniak A; Morales-Narváez E; Merkoçi A, Micro and Nanomotors in Diagnostics. Adv. Drug Deliv. Rev 2015, 95, 104–116. [PubMed: 26408790]
30. Hortelão AC; Carrascosa R; Murillo-Cremaes N; Patiño T; Sánchez S, Targeting 3D Bladder Cancer Spheroids with Urease-Powered Nanomotors. ACS Nano 2019, 13, 429–439. [PubMed: 30588798]
31. Wang H; Pumera M, Micro/Nanomachines and Living Biosystems: From Simple Interactions to Microcyborgs. Adv. Funct. Mater 2018, 28, 1705421.
32. Xu T; Xu L-P; Zhang X, Ultrasound Propulsion of Micro-/Nanomotors. Appl. Mater. Today 2017, 9, 493–503.
33. Campuzano S; Esteban-Fernández de Ávila B; Yáñez-Sedeño P; Pingarrón JM; Wang J, Nano/Microvehicles for Efficient Delivery and (Bio)sensing at the Cellular Level. Chem. Sci 2017, 8, 6750–6763. [PubMed: 29147499]
34. Wang W; Li S; Mair L; Ahmed S; Huang TJ; Mallouk TE, Acoustic Propulsion of Nanorod Motors Inside Living Cells. Angew. Chem. Int. Ed 2014, 53, 3201–3204.
35. Wang W; Castro LA; Hoyos M; Mallouk TE, Autonomous Motion of Metallic Microrods Propelled by Ultrasound. ACS Nano 2012, 6, 6122–6132. [PubMed: 22631222]
36. Ahmed S; Wang W; Bai L; Gentekos DT; Hoyos M; Mallouk TE, Density and Shape Effects in the Acoustic Propulsion of Bimetallic Nanorod Motors. ACS Nano 2016, 10, 4763–4769. [PubMed: 26991933]
37. Esteban-Fernández de Ávila B; Ramírez-Herrera DE; Campuzano S; Angsantikul P; Zhang L; Wang J, Nanomotor-Enabled pH-Responsive Intracellular Delivery of Caspase-3: Toward Rapid Cell Apoptosis. ACS Nano 2017, 11, 5367–5374. [PubMed: 28467853]
38. Hansen-Bruhn M; de Ávila BE-F; Beltrán-Gastélum M; Zhao J; Ramírez-Herrera DE; Angsantikul P; Vesterager Gothelf K; Zhang L; Wang J, Active Intracellular Delivery of a Cas9/sgRNA Complex Using Ultrasound-Propelled Nanomotors. Angew. Chem. Int. Ed 2018, 57, 2657–2661.
39. Esteban-Fernández de Ávila B; Martín A; Soto F; Lopez-Ramirez MA; Campuzano S; Vásquez-Machado GM; Gao W; Zhang L; Wang J, Single Cell Real-Time miRNAs Sensing Based on Nanomotors. ACS Nano 2015, 9, 6756–6764. [PubMed: 26035455]
40. Esteban-Fernández de Ávila B; Angell C; Soto F; Lopez-Ramirez MA; Báez DF; Xie S; Wang J; Chen Y, Acoustically Propelled Nanomotors for Intracellular siRNA Delivery. ACS Nano 2016, 10, 4997–5005. [PubMed: 27022755]
41. Egners A; Erdem M; Cramer T, The Response of Macrophages and Neutrophils to Hypoxia in the Context of Cancer and Other Inflammatory Diseases. Mediators Inflamm. 2016, 2016, 2053646. [PubMed: 27034586]
42. Henze A-T; Mazzone M, The Impact of Hypoxia on Tumor-Associated Macrophages. J. Clin. Invest 2016, 126, 3672–3679. [PubMed: 27482883]
43. Doinikov AA, Acoustic Radiation Pressure on A Rigid Sphere in A Viscous Fluid. Proc. R. Soc. Lond. A 1994, 447, 447–466.
44. Nadal F; Lauga E, Asymmetric Steady Streaming as A Mechanism for Acoustic Propulsion of Rigid Bodies. Phys. Fluids 2014, 26, 082001.
45. Laudien J; Naglav D; Groβ-Heitfeld C; Ferenz KB; de Groot H; Mayer C; Schulz S; Schnepf A; Kirsch M, Perfluorodecalin-Soluble Fluorescent Dyes for The Monitoring of Circulating

Nanocapsules with Intravital Fluorescence Microscopy. J. Microencapsulation 2014, 31, 738–745. [PubMed: 24963954]

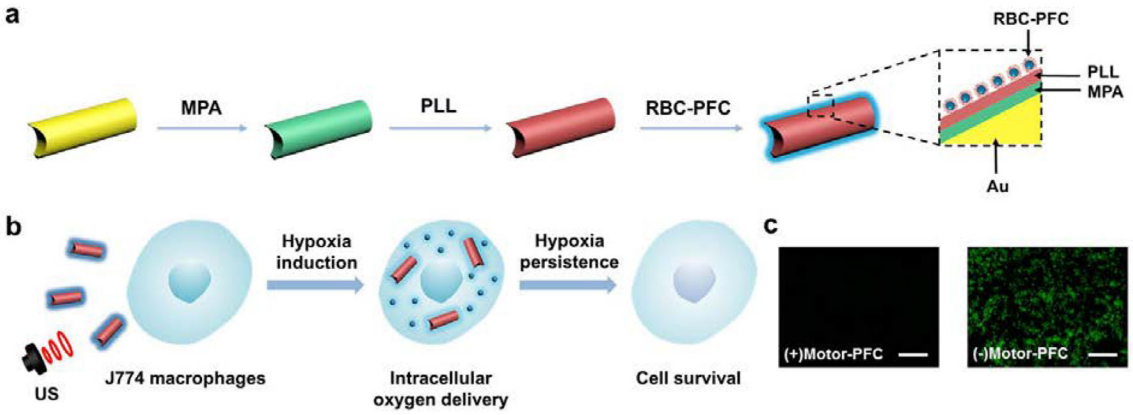

Figure 1. Schematic illustration of a nanomotor-based active O_2 intracellular delivery system.
(a) Loading of RBC-PFC onto AuNW nanomotor surface (Motor-PFC) along with a schematic dissection of the preparation processes: AuNW is first modifed with 3-mercaptopropionic acid (MPA), followed by coating with a poly-L-lysine (PLL) layer. Preformed RBC-PFC nanoemulsions are then attached onto the outer surface of the motors to prepare Motor-PFC. **(b)** Acoustically-assisted intracellular oxygen delivery to J774 macrophages by Motor-PFC, which help cells preserve appropriate oxygen level and maintain viability in hypoxic conditions. **(c)** Intracellular hypoxic stress was indicated by green fluorescence marker, whereas the cells treated by Motor-PFC maintain low hypoxic stress. Scale bars, 100 μm.

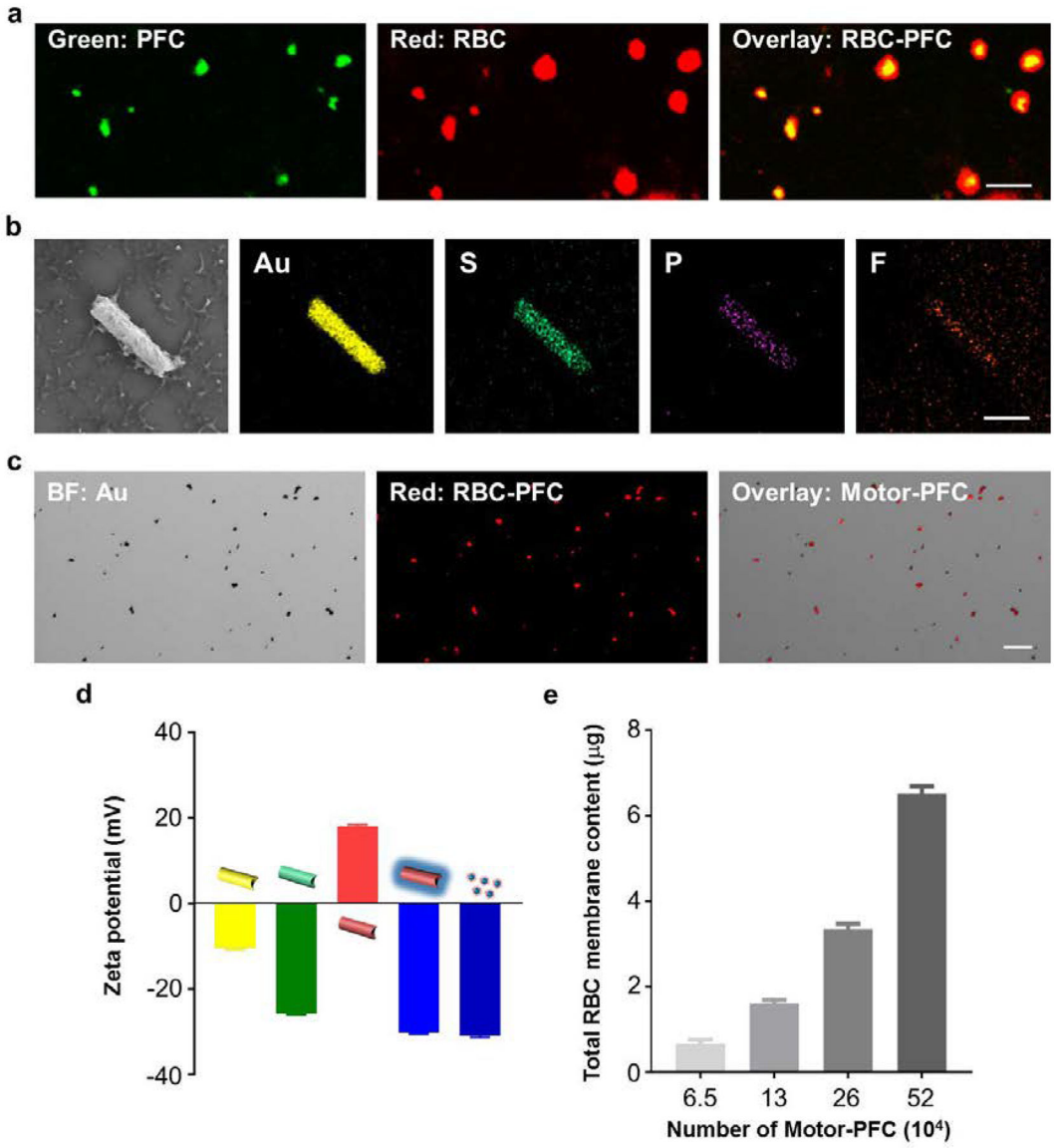

Figure 2. Structural characterization of Motor-PFC.

(a) Confocal fluorescence imaging of dual-labeled RBC-PFC; the RBC membrane was labeled with DiD (red), and the PFC core was labeled with BODIPY (green). Scale bar: 500 nm. **(b)** Scanning electron microscopy (SEM) image of a Motor-PFC and corresponding Energy-dispersive X-ray spectroscopy (EDX) analysis showing the distribution of Au (yellow), S (green), P (purple) and F (orange). Scale bar, 1 μm. **(c)** Bright-field, fluorescent and merged images of a group of Motor-PFC; the RBC membrane was labeled with DiD to help visualization (red). Scale bar, 10 μm. **(d)** Zeta potential of sequential modification of Motor-PFC (from left to right): bare AuNW, MPA-modified AuNW, PLL-modified AuNW, RBC-PFC bound AuNW and free RBC-PFC (n=3, mean ± s.d.). **(e)** Total RBC content on different numbers of Motor-PFC, measured by lipoprotein content from RBC membrane (n=3, mean ± s.d.).

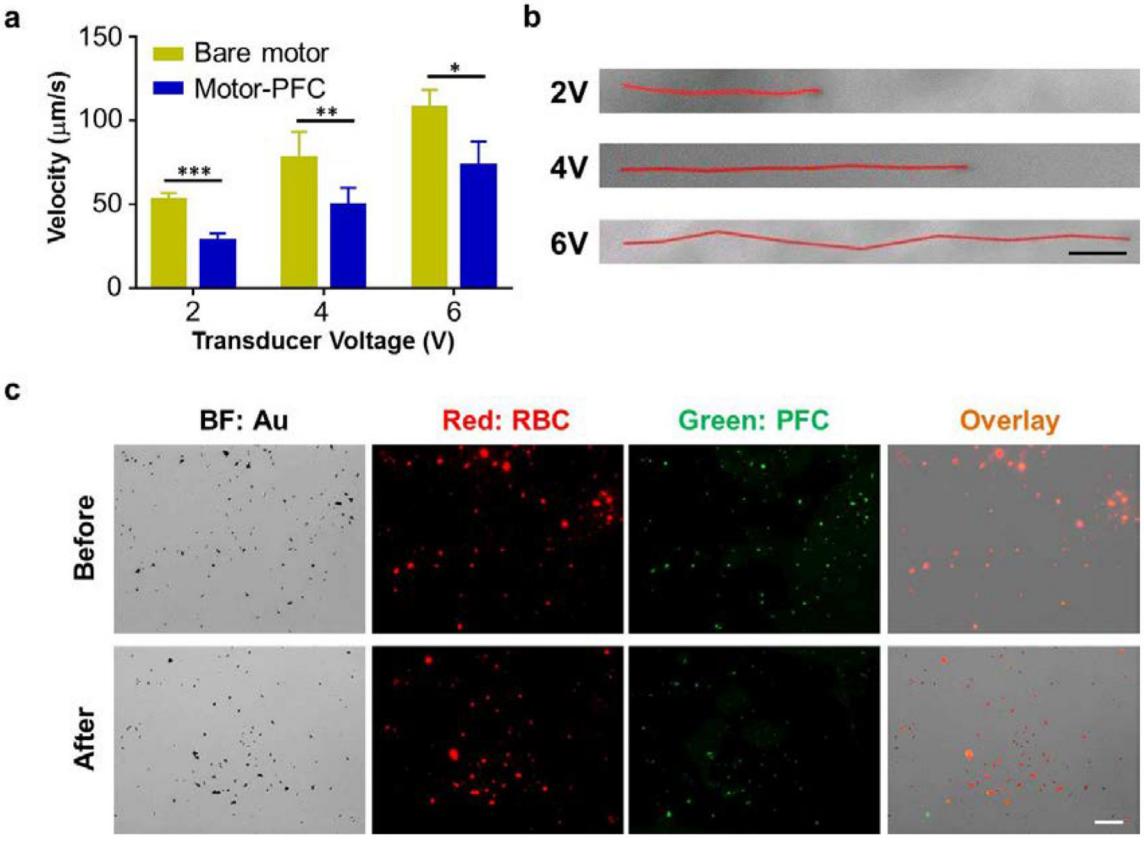

Figure 3. Motion behavior characterization of Motor-PFC.

(a) Comparison of the speed of bare motors and Motor-PFC at different US voltages (2, 4, and 6 V; 2.66 MHz) in water (n=3, mean ± s.d.). *p < 0.05, **p < 0.01, ***p < 0.001; t-test. **(b)** Tracking trajectories of Motor-PFC at different voltages within a 1 s interval in water (Videos S1–S3). Scale bar, 10 μm. **(c)** Verification of the Motor-PFC integrity before (top) and after (bottom) 5 min US propulsion (6 V, 2.66 MHz). The AuNW motor was visualized under brightfield (BF); the RBC membrane was labeled with DiD (red) and the PFC was labeled with BODIPY (green) for fluorescent imaging. Scale bar, 20 μm.

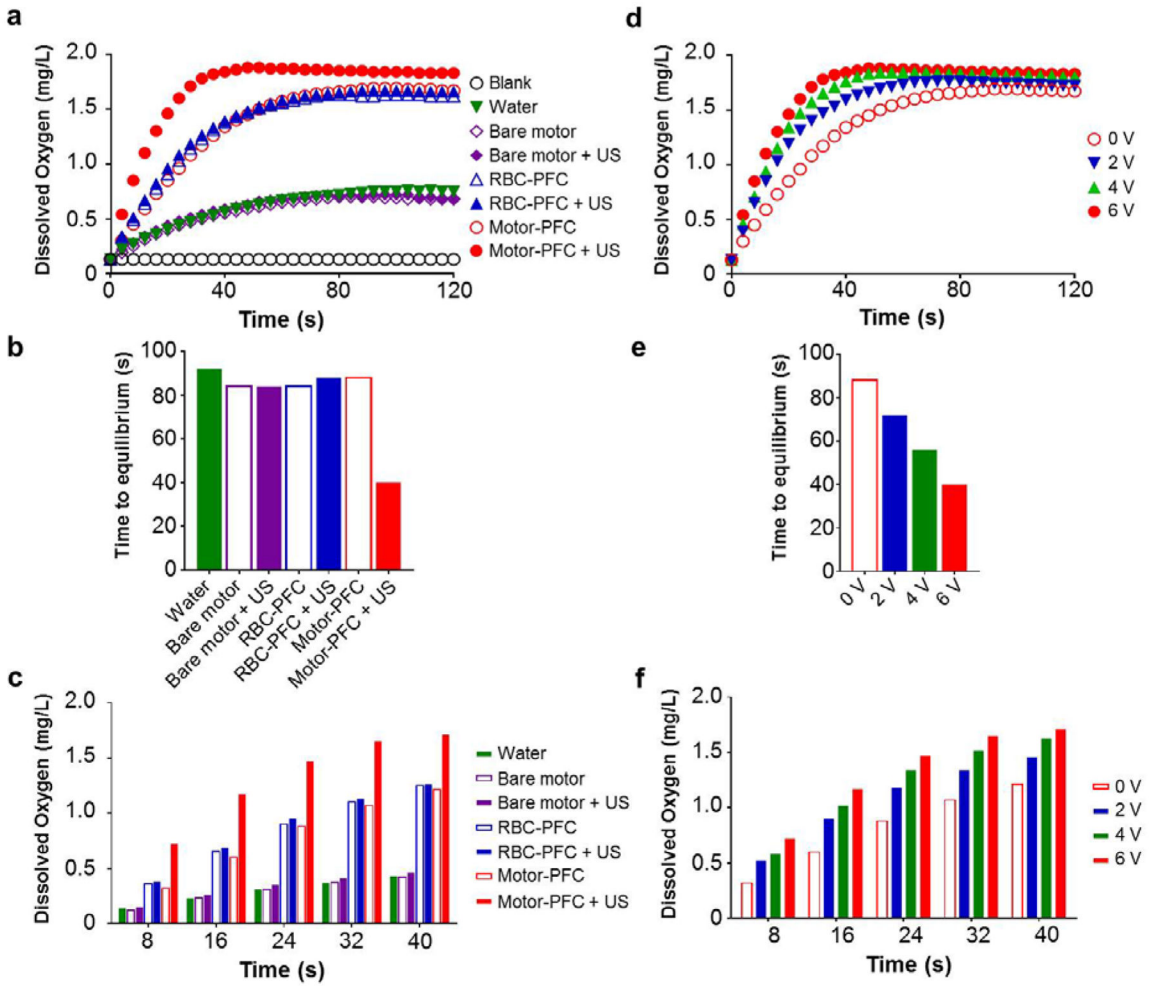

Figure 4. Oxygen delivery kinetics.

(a) Dissolved oxygen kinetics after the addition of oxygenated water, bare motor (with or without US), RBC-PFC (with or without US), Motor-PFC (with or without US) into deoxygenated water. The US field was applied at 6 V. **(b)** Time to reach kinetic equilibrium of each sample indicated in (a). **(c)** Dissolved oxygen levels within first 40 seconds of each sample indicated in (a). **(d)** Dissolved kinetics after the addition of Motor-PFC into deoxygenated water at different US voltages. **(e)** Time to reach kinetic equilibrium of each sample indicated in (d) at different US voltages. **(f)** Dissolved oxygen levels within first 40 second of each sample indicated in (d) at different US voltages. A constant US frequency of 2.66 MHz was used in all experiments.

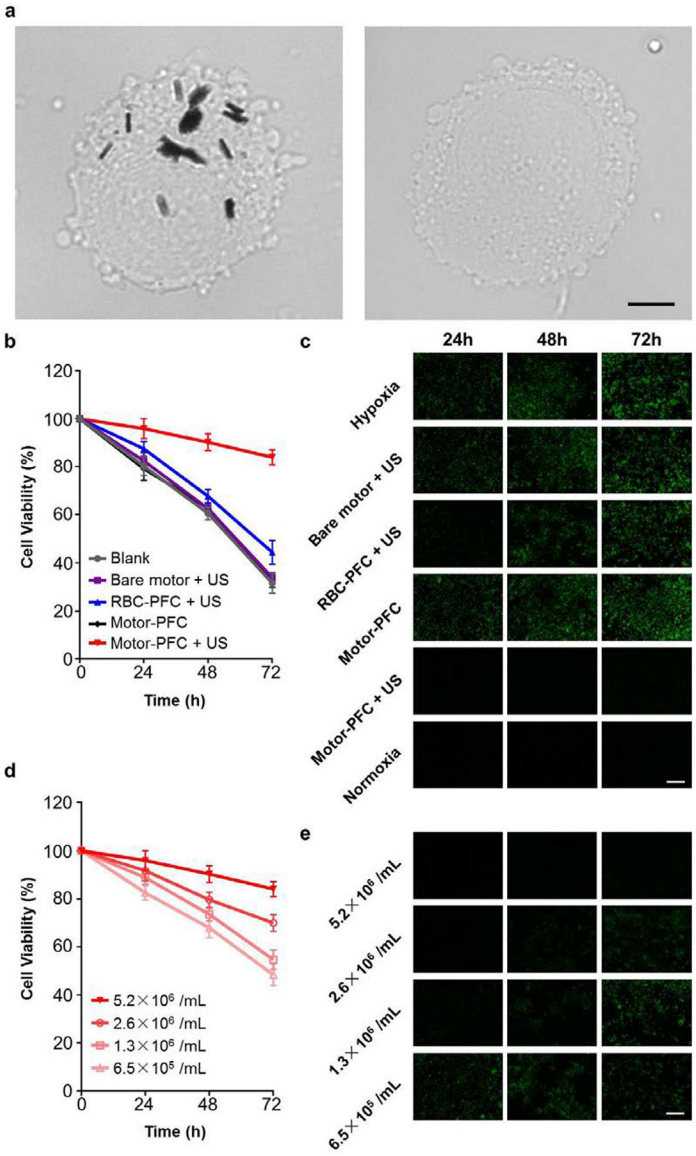

Figure 5. Intracellular oxygen delivery using acoustically-propelled Motor-PFC.

(a) Motor-PFC internalization into J774 cells treated with 5 min US (left) or without US (right); cells imaged under optical microscope. Scale bars, 5 μm. **(b)** Viability of J774 cells after incubation with different treatment conditions and then being subjected to hypoxia. Cells were incubated under hypoxic conditions for 24, 48, or 72 h, and then normalized to corresponding viability in normoxia (n=4, mean ± s.d.). **(c)** Fluorescence microscopy of J774 cells after incubation with different treatment conditions and then being subjected to hypoxia. Cells were labeled with Image-iT Green hypoxia reagent (green) for visualization. Images taken at 24, 48, and 72 h. Scale bar, 100 μm. **(d)** Viability of J774 cells after incubation with Motor-PFC at different input concentrations and then being subjected to hypoxia. Cells were incubated under hypoxic conditions for 24, 48, or 72 h, and then normalized to corresponding viability in normoxia (n=4, mean ± s.d.). **(e)** Fluorescence microscopy of J774 cells after incubation with Motor-PFC at different input concentrations

and then being subjected to hypoxia. Cells were labeled with Image-iT Green hypoxia reagent (green) for visualization. Images taken at 24, 48, and 72 h. Scale bar, 100 μm.